Available online at www.sciencedirect.com
SCIENCE DIRECT®
Composites Science and Technology 65 (2005) 883–897
COMPOSITES SCIENCE AND TECHNOLOGY
www.elsevier.com/locate/compscitech

Intrinsic parameters in the fracture of carbon/carbon composites

Konstantinos G. Dassios [a,b,c], V. Kostopoulos [b,c,*], M. Steen [a]

[a] Institute for Energy, Joint Research Centre, European Commission, Westerduinweg 4, 1755 LE Petten, The Netherlands
[b] Department of Mechanical Engineering and Aeronautics, Institute of Chemical Engineering and High Temperature Chemical Processes/FORTH, Applied Mechanics Laboratory, Patras University Campus, University of Patras, Patras 26500, Greece
[c] Foundation of Research and Technology Hellas, Institute of Chemical Engineering and High Temperature Processes, Stadiou str., Platani, GR-26500, Patras, Greece

Received 16 December 2002; received in revised form 27 April 2004; accepted 10 October 2004
Available online 7 January 2005

Abstract

The *R*-curve, bridging stress profile and the corresponding bridging law of C/C woven composites were calculated for two different specimen configurations: compact tension (CT) and double-edge-notch (DEN). Monotonic tensile loading as well as cyclic loading was performed on CT specimens and the *R*-curve was evaluated from the change of specimen compliance in the presence and absence of the bridging zone by quantifying the total damage in the material through an effective crack length approach. The bridging stresses and laws for the DEN specimens tested under monotonic tension were calculated directly through the elastic correction of the measured displacement. The comparison of the *R*-curves and bridging laws between the two configurations was performed after identification of a common damage extent measure, the local crack opening displacement. The rising part of the *R*-curve was found similar for the two configurations, with the mean initiation and plateau values being $R_0 \sim 1.3$ and $R_\infty \sim 9.5$ kJ/m^2, respectively. In contrast, the bridging laws evaluated for the two configurations were in disagreement. It was concluded that the investigated material, although characterised as Class-III in the literature, exhibits crack growth and bridging, however of a Small rather of a large scale and that the calculated *R*-curve can serve as an intrinsic parameter that characterises the fracture behaviour of the material independently of configuration, and – thus – independently of dimensions and geometry.
© 2004 Elsevier Ltd. All rights reserved.

Keywords: A. Ceramic-matrix composites; B. Fracture; C. Crack; Fibre bridging

1. Introduction

The prominent mechanical properties and the excellent fracture behaviour of continuous fibre-reinforced ceramic-matrix and carbon/carbon composites (CFCCs and C/C) under high thermal and mechanical loads place them today among the ideal candidate materials for structural applications for use at conventional and high temperatures. Their increased fracture resistance and their ability to retain strength in the presence of holes and notches that results from active stress redistribution mechanisms is deployed today for maintaining the toughness and durability of structural components that must perform reliably under severe thermo-mechanical conditions. Such applications include the braking systems of high-speed trains and aircraft as well as rocket engine parts. As an example, one of the most widely used materials in this class is the carbon/carbon composite family; with protective top layer coatings to prevent oxygen attack at temperatures above 500 °C, carbon/carbon composites can perform to temperatures up to 2500 °C without important degradation of properties [1].

Carbon/carbon as well as most CFCCs consist of brittle matrices and high mechanical performance

* Corresponding author. Tel.: +30 61 997 234; fax: +30 61 992 644.
E-mail addresses: cdassios@mech.upatras.gr (K.G. Dassios), kostopoulos@mech.upatras.gr (V. Kostopoulos).

0266-3538/$ - see front matter © 2004 Elsevier Ltd. All rights reserved.
doi:10.1016/j.compscitech.2004.10.021

long-fibre reinforcements. The fracture behaviour is associated with the development and evolution of matrix cracks and a corresponding damage zone (e.g. [2]). Depending on their constituents and their internal structure, CFCCs can exhibit three major damage mechanisms [3]. Fracture associated with internal fibre failure and a distinct matrix crack represents "Class I" composite behaviour whereas in "Class II" behaviour the stresses are redistributed around multiple matrix cracks and the reinforcing phase remains intact. "Class III" composites exhibit multiple unordered shear matrix cracking, and stresses are redistributed internally within a shear damage zone.

The damage zone in Class I and Class II composites is believed to consist of two parts: the matrix process zone ahead of the crack tip and the bridging zone behind the crack tip. In the matrix process zone a complex set of phenomena take place concurrently; such phenomena may include matrix microcracking, fibre/matrix interfacial debonding and transformation toughening. In the bridging zone the cracked matrix is bridged by intact and/or failed fibres, which debond, slip and pull-out. The role of the bridging zone in the fracture resistance is of particular importance as the bridging fibres are responsible for opposing further crack propagation by obstructing crack opening, thus reducing the crack driving force and contributing in that way significantly to the resistance of the material to further fracture. The damage zone is believed to develop around the crack tip during the early fracture stages and, after it has reached a steady state, propagates in a self-similar manner along with the crack tip. In Class III materials the fracture resistance is more a result of the stress redistribution micro-mechanisms active in the shear damage zone rather than the bridging effect [3]. Although the micro-mechanical fundamentals of such a damage zone differ from the mechanisms active in Class I and II composites, it has been shown [4] that the two behaviours can be unified using an "effective crack length" approach to quantify the shear Class III damage by means of type-I and II damage (distinct cracks).

In the presence of a damage zone, the fracture behaviour is classically characterised by a resistance curve instead of a fracture toughness value. In fibre-reinforced composites, the well-established rising crack growth resistance with increasing crack extension (R-curve) is a direct result of crack bridging. When the size of the bridging zone is much smaller in length than the characteristic specimen dimension, the R-curve can be regarded as an intrinsic material characteristic and can be used to uniquely describe the fracture behaviour of the material, independently of its geometry and dimensions. However, this is not the case in many CFCCs, where the bridging zone size is within the order of magnitude of a characteristic specimen dimension. This situation, commonly known as large scale bridging (LSB), renders the R-curve a material-extrinsic property that depends upon the specimen geometry and dimensions [5]. Since design procedures must be straightforward and robust and need simplified and easy to implement models that provide acceptable precision, the development of intrinsic fracture characteristics for CFCC materials shows a unique need and challenge. To that end, a bridging law approach has been proposed [5,6] that correlates the local bridging stress to the local crack opening displacement (COD), i.e. the local opening of the crack flanks. The bridging law concept is in a sense a measure of the closure traction normalised to the local geometrical and dimensional characteristics, and as such it has been proposed to serve as a basic material law [6–10].

A number of studies have focused on measurement of the bridging law for composite materials. Different approaches include the calculation of the idealised bridging law from micromechanical models [11] and the experimental measurement of real bridging laws. Sorensen and Jacobsen [8] used a new approach based on the application of the J-integral to measure the bridging law characteristics of carbon fibre/epoxy matrix DCB specimens tested in pure bending while simultaneously recording the end-opening and the crack advance (optically through replicas). In that study the crack growth resistance was found to be independent of the specimen dimensions when plotted versus crack opening, δ, and a bridging law of the form of $\sigma \propto \delta^{-1/2}$ was calculated, where σ refers to bridging stress. In a subsequent study [10] this calculated bridging law was used to model the R-curve of the same material. Mai and Hu [12] assumed a linear relation between the crack opening displacement and the distance from the crack tip in order to evaluate the bridging stress profile from tests on compact tension (CT) specimens. This approach, coupled with a compliance-based method has been successfully applied by Kostopoulos and Markopoulos [4] to quantify the fracture behaviour of carbon/carbon CT specimens of different thickness tested under monotonic and cyclic loading conditions. Rouby and co-workers [7] proposed a straightforward procedure for the evaluation of macro-mechanical bridging stresses and bridging laws in double-edge-notch (DEN) specimens that involves a simple de-convolution of the stress-strain data into an intact/bridging-fibre and a fibre-pull-out contribution. Due to the minimal number of assumptions associated with this procedure, the DEN test is known today as the most direct manner to measure bridging loads, stresses and laws at the macroscale.

While the quantification of the R-curve behaviour, of the bridging stress field and of bridging laws has been studied extensively over the last years, knowledge of intrinsic fracture parameters of CFC composites is still limited. A characteristic example are C/C composites where multiple shear cracks appear in the matrix during

composite fracture and result in a complex bridging zone of dimensions that can hardly be measured. On the other hand, there are indications that shear cracking coexists with distinct matrix cracks forming and growing in such materials [9]. As a result, it is currently unverified whether C/C composites are purely Class III materials and whether their fracture behaviour is compatible with LSB or SSB (small scale bridging) conditions. Consequently, material intrinsic fracture parameters are currently unknown for such composites. The goal of this study is to investigate the fracture behaviour of a woven C/C composite of different configurations with emphasis on the identification of appropriate fracture parameters that remain unchanged when the dimensional and geometrical characteristics of the specimens are modified. This is achieved through a series of tests on CT and DEN specimens and the subsequent analysis of the *R*-curve, of the bridging stress field and of the corresponding bridging law for each configuration. The identification of material-intrinsic properties, that characterise the fracture behaviour of the composite independently from its dimensions *and* its geometry, was performed in this study under the principle that *geometric intrinsicality is a necessary and sufficient condition for dimensional intrinsicality*, while the reverse does not always hold. In other words, a fracture property that remains unchanged for different configurations, will also remain unchanged for different scaling variations of the same configuration.

In this study, the bridging stresses for the CT configuration are evaluated following the concept developed by Mai and Hu [12] and Kostopoulos and Markopoulos [4], which quantifies the change in compliance when bridging is present or not. This approach is very useful for complex systems like the woven composite where the effective crack extension can hardly be measured experimentally. The evaluation of bridging stresses in the DEN specimens performed in this study follows the procedure presented by Rouby and co-workers [7].

2. Experimental

2.1. Materials, specimens and testing

The composite tested is a commercially available 2D carbon/carbon laminate manufactured by Schunk Kohlenstofftechnik GmbH (Germany). Orthogonally woven eight-harness satin weave fabric of high modulus carbon fibres reinforces the laminates. The laminates are stacked together in a 0°/90° orientation. The production phase involved a series of carbonisation steps at 800 °C and re-impregnation with phenolic resin with a final graphitisation post-treatment at 2100 °C. This resulted in dense C/C plates with less than 10% porosity and a 60% fibre volume fraction. The bulk density of the material is 1.49 g cm^{-3}. CT and DEN specimens were machined from a composite plate with a thickness of 3.0 mm.

Schematic representations of typical CT and DEN specimens used in this study are presented in Fig. 1. The principal specimen dimension, *W*, is 65 and 10.5 mm for the CT and DEN specimens, respectively. The CT specimens were machined in the erosion chamber of a high precision wire-cut Electrical Discharge Machine (Fanuc Robocut Alpha-1c, Series 16-W) using a wire diameter of 250 μm. The same equipment was used to machine the notches in the CT specimens. DEN specimens were cut from the composite plate using a 150 μm thick diamond disk that was also used for the preparation of the different notches. Mechanical testing was performed in extension control on a Schenck Trebel RMC100 mechanical frame equipped with a 63 kN load cell. The crosshead velocity of the testing machine was kept constant at 0.1 mm/min for the CT specimens and 0.01 mm/min for the DEN specimens where crack propagation was anticipated to evolve faster.

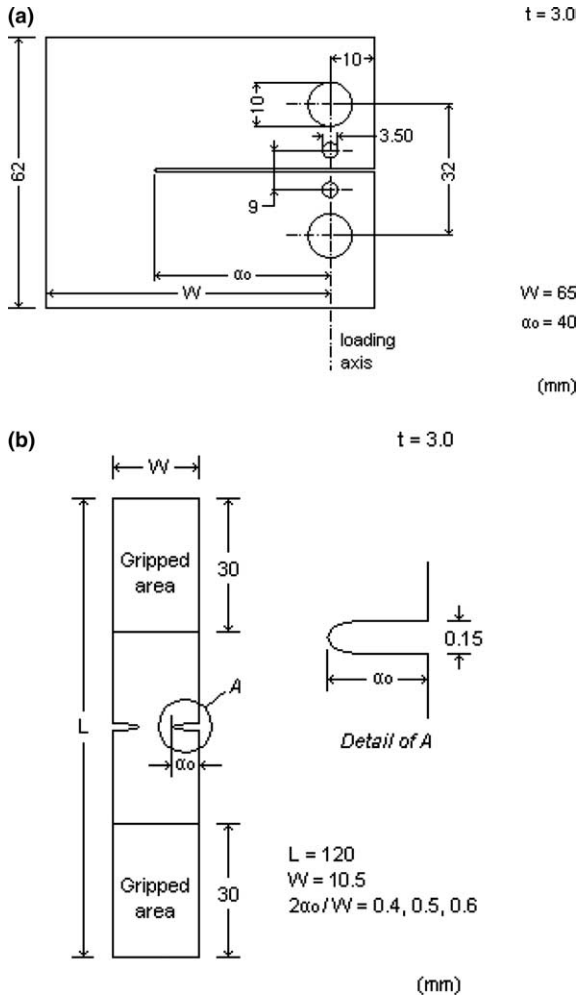

Fig. 1. Dimensional characteristics of the C/C specimens: (a) CT configuration and (b) DEN configuration.

For the DEN specimens, displacement was measured directly by fixing an extensometer (gauge length 25 mm) to one side. For CT specimens, the crack mouth opening was measured using a COD transducer equipped with two double fork-like legs (Fig. 2). The legs were mounted on the specimen between two detachable cylindrical pins fitted in 3.5-mm diameter holes on the specimen's loading axis, on either side of the notch. The transducer's force restoring spring kept the fixture fixed between the two pins. The upper leg pair was equipped with a symmetric 90° groove on both legs which allowed for exact positioning while the lower leg pair could slide on the pin surface. In this manner, the COD measuring fixture had two symmetric rotational and two symmetric translational points of contact instead of two fixed, non-rotational contact points used in other studies.

2.2. CT specimens – quasi-static tensile loading

2.2.1. Establishing the general properties

To determine the maximum load capacity, the extent of the elastic region and the general mechanical behaviour of the materials, monotonic tensile loading up to failure was performed on one CT specimen with an initial notch length of 40 mm from the loading axis. A typical load–displacement curve is presented in Fig. 3.

2.2.2. Compliance calibration

The change in compliance C (expressed with respect to crack opening displacement) in the absence of crack-face bridging was calibrated as a function of the (un-bridged) crack length by testing specimens with initial machined notches of various lengths under monotonic tensile loads within the elastic regime, i.e. up to 1/3 of the linear load capacity obtained in the test described in the previous section. Within this load range the material behaviour is reversible as damage has not developed and the compliance, i.e. the inverse slope of the load–COD graph, can be directly related to the notch length. One specimen was used to perform 12 tests with notch lengths ranging between 0 and 55 mm with a step of 5 mm. Fig. 4 shows the load–COD traces of the tests.

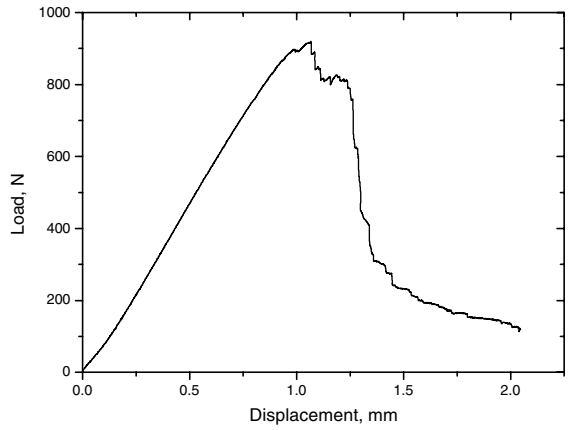

Fig. 3. Typical load–displacement curve obtained on C/C CT specimen.

The compliance, C, versus (un-bridged) crack length, α (Fig. 5) was fitted with a function of the form $C(\alpha) = b\alpha/(d-\alpha)$ under the χ^2 reduction criterion. This function exhibits an asymptote for $\alpha = d$. An unconstrained fit to the data of Fig. 5 gives $d = 60$ mm (solid line) but a value of $d = W(=65$ mm) proves more realistic since for $d = W$ the fitting function has the physical meaning that infinite values of compliance are reached when no material exists to support the applied load. For the latter case it is evident that the last two experimental points of the compliance calibration curve in Fig. 5 are not on the said curve and this is the result of the effect of the compressive zone which has developed at the rear face of the CT specimen and results in lower values for the compliance. The parameter b is a material-dependent scaling factor, with a value equal

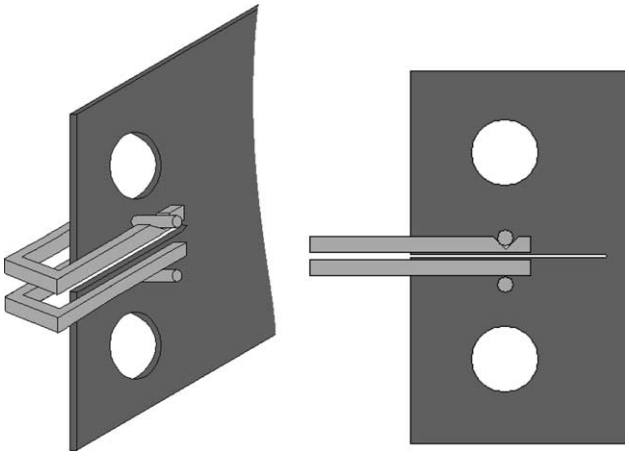

Fig. 2. Measurement of the crack opening displacement along the loading axis of the CT specimens.

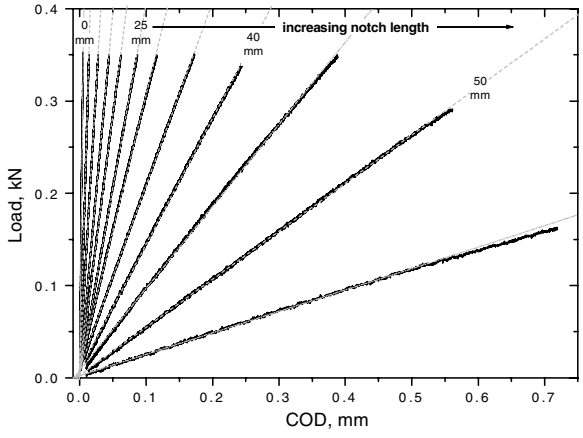

Fig. 4. Compliance calibration of the C/C CT specimen. The load as a function of COD for different notch lengths.

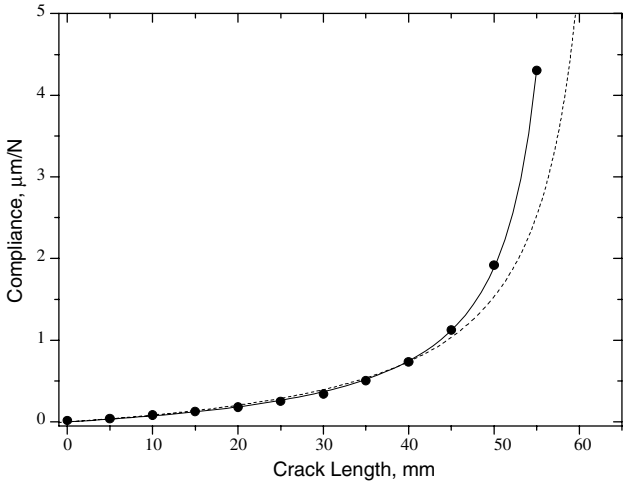

Fig. 5. Compliance calibration of the C/C CT specimen. The solid line is an unconstrained fit while the dashed line assumes that the compliance reaches an infinite value at a crack length equal to the width of the specimen (asymptote at $d = W$).

to the compliance when the remaining intact ligament equals the crack length.

2.3. CT specimens – cyclic loading

Cyclic testing was performed on CT specimens with an initial notch length of 40 mm from the loading axis. Loading/unloading/reloading cycles were generated automatically from the frame-controlling software after manual input of the extension-based algorithm: cycling commenced at a crosshead displacement of 0.5 mm, a value that corresponds to a pre-maximum-load instance (determined from the quasi-static tensile test to failure); the specimen was then unloaded up to full relaxation (zero force) and loaded again. The subsequent loop commenced after the crosshead had extended an additional 0.05 mm from the starting displacement of the previous cycle. The final loop commenced at a crosshead displacement of 1.5 mm in order that a total of 20 cycles were performed for each specimen. The time, displacement, load (P) and COD where recorded simultaneously. A typical P–COD curve obtained is shown in Fig. 6. The broadening of the unloading/reloading cycles manifests a hysteresis effect that is directly related to the extent of irreversible damage caused to the material.

2.4. DEN specimens – monotonic tensile loading

DEN specimens of a fixed width of 10.5 mm and symmetric initial notches of 2.1, 2.6 and 3.1 mm were tested under monotonic tensile loading. A typical load–displacement curve is presented in Fig. 7. The failure of the DEN specimens was rapid and data acquisition was sparse after a critical load level.

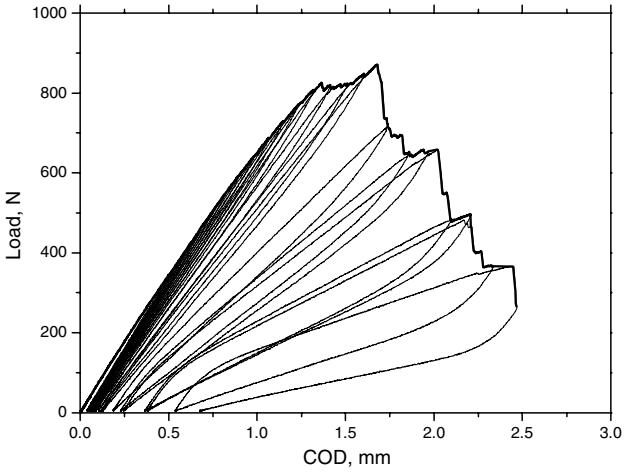

Fig. 6. Typical load (P)–COD curve for the C/C CT specimen under cyclic loading.

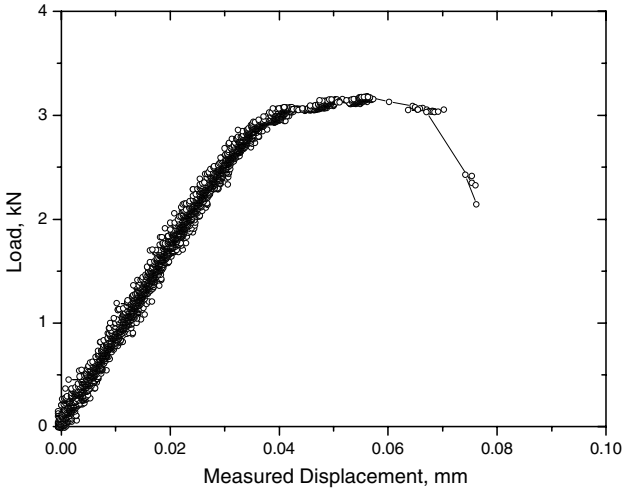

Fig. 7. Typical load–displacement curve for a DEN specimen under monotonic tensile loading ($2\alpha_0/W = 0.5$).

3. CT specimens: *R*-curve methodology and evaluation

Under the assumption of non-linear non-elastic fracture behaviour, after the maximum load has been attained, irreversible damage accumulates in the specimen. The active damage mechanisms include micro-mechanical contributions such as interfacial failure, which lead to fibre/matrix debonding and debris effects, as well as macro-mechanical phenomena, such as fibre bridging and pullout.

3.1. R-Curve evaluation methodology – cyclic loading

3.1.1. Calculation of the effective crack length

A typical case of non-linear, non-elastic fracture behaviour is presented schematically in Fig. 8. Beyond a given load, irreversible damage evidenced by residual

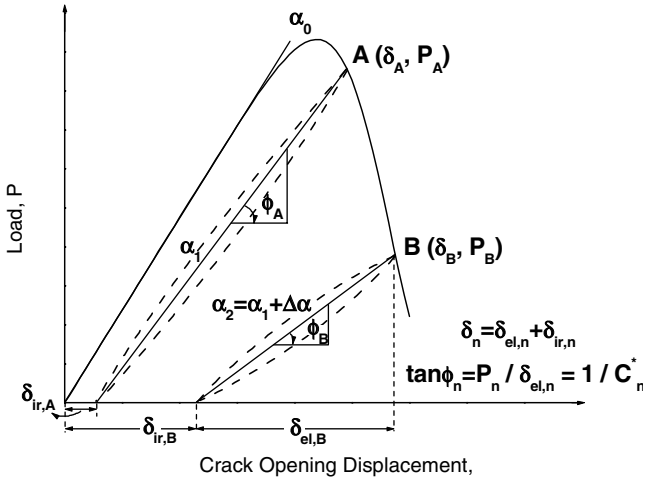

Fig. 8. Typical non-linear non-elastic fracture behaviour.

crack opening accumulates at each unloading/reloading cycle. The total crack opening displacement δ_n of the nth cycle is the sum of an elastic, $\delta_{\mathrm{el},n}$, and an irreversible contribution, $\delta_{\mathrm{ir},n}$.

The inverse unloading slope defines the *modified compliance* at the nth cycle which is the compliance of the material in the presence of crack-face bridging:

$$C_n^* = \frac{\delta_{\mathrm{el},n}}{P_n}. \tag{1}$$

A semi-empirical recurrence formula has been proposed [4,12] to correlate the modified compliance calculated at the nth cycle with the effective crack extension $\Delta\alpha_n = \alpha_n - \alpha_0$:

$$\Delta\alpha_n = \Delta\alpha_{n-1} + \frac{W - \Delta\alpha_{n-1}}{2}\frac{C_n^* - C_{n-1}^*}{C_n^*}, \quad n = 1,2,\ldots, \tag{2}$$

where $\Delta\alpha_0 = 0$.

Integrating and rearranging, Eq. (2) can be re-written in a functional form as

$$C^*(\alpha) \approx \frac{1}{(W-\alpha)^2}. \tag{3}$$

In a previous section (compliance calibration) the compliance for the case where bridging is absent varied with crack length according to:

$$C(\alpha) = \frac{b\alpha}{W-\alpha}. \tag{4}$$

Differentiating Eqs. (3) and (4) we obtain:

$$\frac{\mathrm{d}C^*(\alpha)}{\mathrm{d}\alpha} \approx \frac{2}{(W-\alpha)^3} \tag{5}$$

and

$$\frac{\mathrm{d}C(\alpha)}{\mathrm{d}\alpha} = \frac{bW}{(W-\alpha)^2}. \tag{6}$$

Comparing Eqs. (5) and (6) we observe that the compliance in the presence of bridging increases with crack length at a much smaller rate – of one order less – than when bridging is not present. This restrained increase of compliance is directly related to the presence of a bridging zone where the stresses carried by the bridging fibres oppose further opening of the crack flanks.

3.1.2. Non-linear elastic and irreversible energy release rates

The total mechanical energy for crack growth supplied externally to the specimen is consumed partly for the creation of new crack surfaces, while another part is dissipated through additional phenomena that follow the cracking such as fibre sliding and pull-out, debris formation, interface damage. The total energy W_n needed for the formation of a crack of a given length α_n is the sum of:

$$W_n = \Gamma_n + U_{\mathrm{el},n} + U_{\mathrm{ir},n}, \tag{7}$$

where Γ_n is the energy needed to create a crack surface $S_n = t \times \alpha_n$, t is the specimen thickness, $U_{\mathrm{ir},n}$ is the energy needed for additional irreversible damage and $U_{\mathrm{el},n}$ is the energy provided to the specimen for elastic deformation (Fig. 9(a)).

Accordingly, the total energy needed for an already formed crack to grow by an increment of $\Delta\alpha_n$ is ΔW_n and is the sum of three contributions: (1) $\Delta\Gamma_n$, the energy needed to create a new crack surface $\Delta S_n = t \times \Delta\,\alpha_n$, (2) $\Delta U_{\mathrm{ir},n}$, the energy consumed in additional irreversible phenomena during the incremental crack growth and (3) $U_{\mathrm{el},n}$ the elastic energy (Fig. 9(b)).

Analytically, $U_{\mathrm{el},n}$ and $U_{\mathrm{ir},n}$ can be calculated using Eq. (1) as follows:

$$U_{\mathrm{el},n} = \frac{1}{2}P_n\delta_{\mathrm{el},n} = \frac{1}{2}P_n^2 C_n^*, \tag{8}$$

$$U_{\mathrm{ir},n} = \frac{1}{2}P_n\delta_{\mathrm{ir},n}. \tag{9}$$

For the formation of a crack increment $\Delta\alpha_n$, a portion λ_n of the total mechanical energy input W_n is consumed by the damage mechanisms that produce $\delta_{\mathrm{ir},n}$:

$$\lambda_n = \frac{\Delta U_{\mathrm{ir},n}}{\Delta W_n}, \tag{10}$$

where W_n is the area under the P–δ curve up to the nth cycle, or:

$$W_n = \int_0^{\delta(\alpha_n)} P(\delta)\,\mathrm{d}\delta. \tag{11}$$

The irreversible energy release rate Φ_{ir} is the rate of change of the irreversible energy contribution, $U_{\mathrm{ir},n}$ consumed during the creation of the crack surface ΔS_n. Taking into consideration, Eqs. (10) and (11), Φ_{ir} is given by the equation:

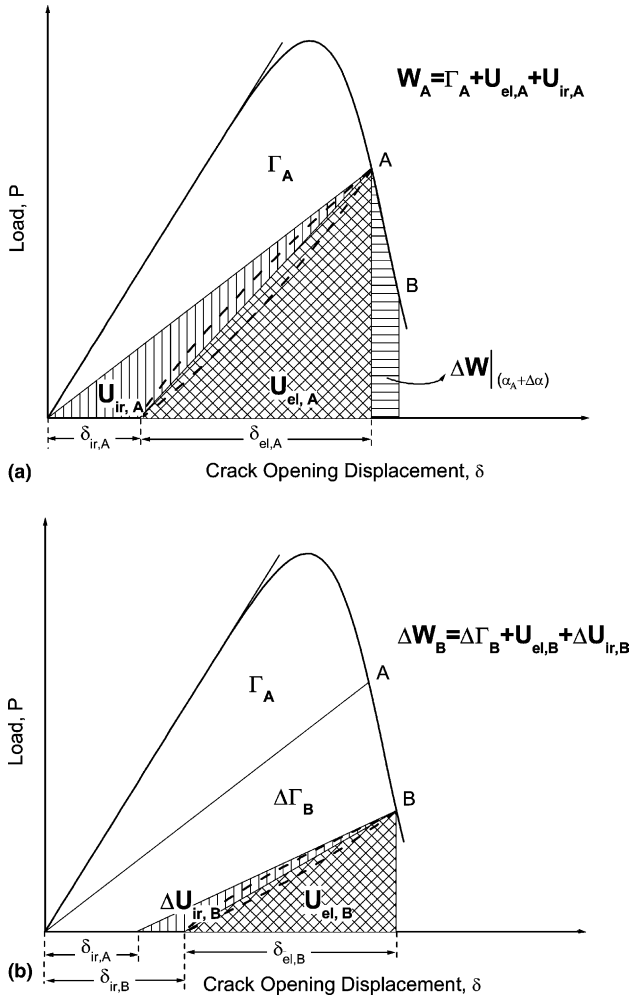

Fig. 9. Different energy contributions consumed during crack propagation. $\Delta\Gamma_n$ represents, at each cycle, the additional energy needed for the creation of a new crack surface $\Delta S_n = t \times (\alpha_n - \alpha_{n-1})$.

$$\Phi_{\mathrm{ir}} = \lim_{\Delta\alpha_n \to 0}\left(\frac{\Delta U_{\mathrm{ir},n}}{\Delta S_n}\right) = \lim_{\Delta\alpha_n \to 0}\left(\frac{\Delta U_{\mathrm{ir},n}}{t\Delta\alpha_n}\right) = \frac{\mathrm{d}U_{\mathrm{ir},n}}{t\,\mathrm{d}\alpha} = \frac{1}{t}\frac{\mathrm{d}}{\mathrm{d}\alpha}(\lambda_n W_n) = \lambda_n \frac{P_n}{t}\frac{\mathrm{d}\delta}{\mathrm{d}\alpha}. \quad (12)$$

The elastic non-linear energy release rate G_{R}^* is the rate of change of the energy consumed in the creation of the crack surface ΔS_n. Taking into consideration, Eq. (7), G_{R}^* is given by the equation:

$$G_{\mathrm{R}}^* = \lim_{\Delta\alpha_n \to 0}\left(\frac{\Delta\Gamma_n}{\Delta S_n}\right) = \lim_{\Delta\alpha_n \to 0}\left(\frac{\Delta(W_n - U_{\mathrm{el},n} - U_{\mathrm{ir},n})}{t\Delta\alpha_n}\right) = \frac{1}{t}\left[\left(\frac{1-\lambda_n}{\lambda_n}\right)\frac{\mathrm{d}U_{\mathrm{ir},n}}{\mathrm{d}\alpha} - \frac{\mathrm{d}U_{\mathrm{el},n}}{\mathrm{d}\alpha}\right]. \quad (13)$$

Using Eqs. (8) and (12), Eq. (13) can be re-written as

$$G_{\mathrm{R}}^* = \frac{1}{t}\left[(1-\lambda_n)\frac{P_n\,\mathrm{d}\delta}{\mathrm{d}\alpha} - P_n C_n^* \frac{\mathrm{d}P_n}{\mathrm{d}\alpha} - \frac{P_n^2}{2}\frac{\mathrm{d}C_n^*}{\mathrm{d}\alpha}\right]. \quad (14)$$

The total crack growth resistance, R, is given by:

$$R = \Phi_{\mathrm{ir}} + G_{\mathrm{R}}^* = \frac{1}{t}\left[\frac{P_n\,\mathrm{d}\delta}{\mathrm{d}\alpha} - P_n C_n^* \frac{\mathrm{d}P_n}{\mathrm{d}\alpha} - \frac{P_n^2}{2}\frac{\mathrm{d}C_n^*}{\mathrm{d}\alpha}\right]. \quad (15)$$

In practice, for the calculation of G_{R}^*, Φ_{ir} and R one needs to perform the following steps:

☐ For each cycle:

- Record the P_n, δ_n, $\delta_{\mathrm{el},n}$ and $\delta_{\mathrm{ir},n}$ values (Fig. 8).
- Calculate the modified compliance C_n^* (through Eq. (1)).
- Apply the iterative formula (Eq. (2)) to calculate the effective crack extension corresponding to the value of C_n^*.
- Calculate the total energy input W_n using Eq. (11) (by integration of the P–δ curve up to the value of δ that corresponds to the cycle), the irreversible energy $U_{\mathrm{ir},n}$ using Eq. (9) and the corresponding value of λ_n using Eq. (10).

☐ Calculate the functions $P_n(\alpha)$, $\delta_n(\alpha)$, $C_n^*(\alpha)$ for all cycles as well as their derivatives with respect to α.

☐ And, again for each cycle:

- Apply Eqs. (12) and (14) to calculate Φ_{ir} and G_{R}^*, respectively.
- Calculate R by addition of Φ_{ir} and G_{R}^* (Eq. (15)).

As discussed in Section 1, the bridging stresses develop in a zone behind the crack tip during the early fracture stages. After the process zone has fully developed (reaching a steady-state profile) it propagates self-similarly following the path of the crack tip. The length of the fully developed bridging zone, A, is defined as that crack extension where the bridging stress profile has reached a steady state; the length A can be determined from the R-curve as the extension that corresponds to the first instance in the steady state of R.

3.2. R-Curve evaluation for CT specimens

The procedure presented in Section 3.1 was followed to evaluate the R-curve for the CT tests. The load P_n, the crack opening displacement $\delta_n = \delta_{\mathrm{el},n} + \delta_{\mathrm{ir},n}$ and the modified compliance C_n^* of each cycle are plotted as functions of crack extension in Figs. 10(a)–(c) where only the cycles contributing in the development and the initial self-similar propagation stages of the bridging zone are presented (i.e. omitting the results from the unloading/reloading cycles that are affected by the compressive zone at the rear side of the specimen).

Additionally, the total and irreversible energy contributions were calculated to determine the ratio of the irreversible energy to the total energy input, λ_n, for every cycle.

The elastic non-linear energy release rate G_R^*, the irreversible energy release rate Φ_{ir}, and the total crack growth resistance R were calculated through Eqs. (12), (14) and (15), respectively, and are plotted as functions of crack extension in Figs. 11(a)–(c).

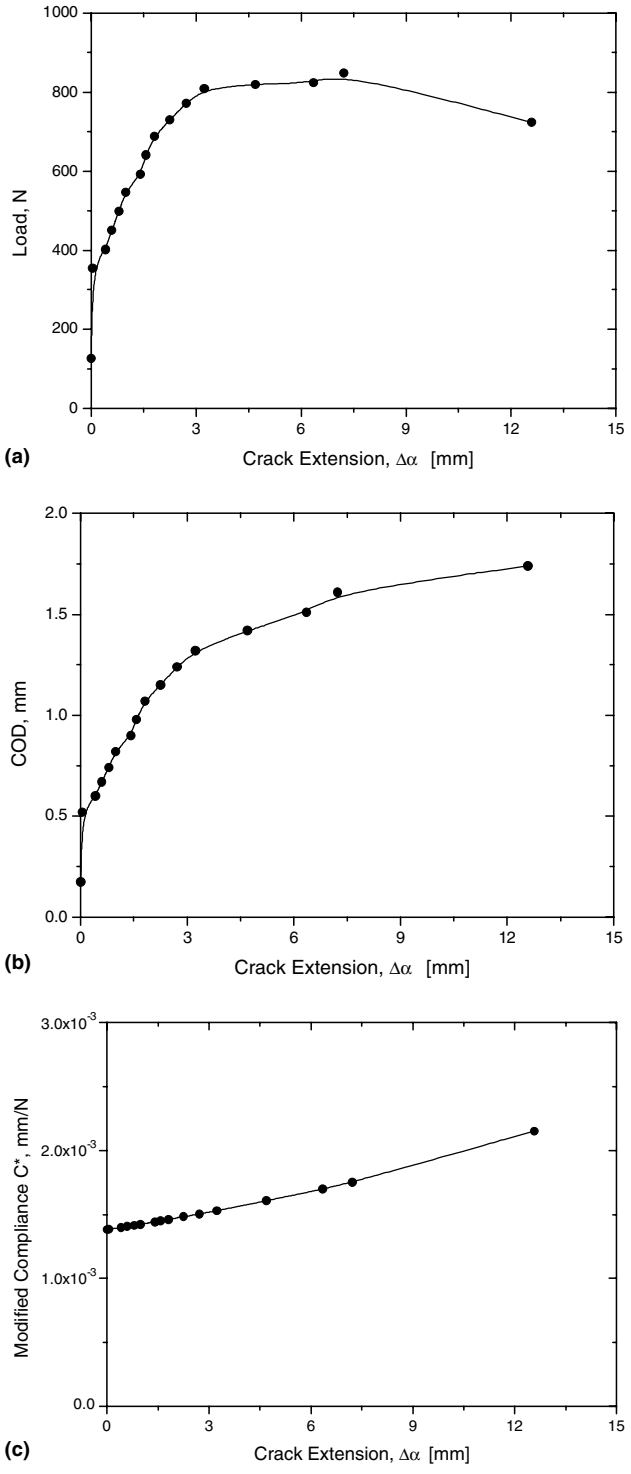

Fig. 10. (a)–(c) The load P_n, crack opening displacement δ_n and modified compliance C_n^* dplotted as a function of the crack extension, $\Delta\,\alpha_n$, for unload–reload cycles.

The R-curve of Fig. 11(c) exhibits "overshoot", i.e. a transient fluctuation around the region of ca. 1.5 mm of crack extension. This phenomenon has also been observed in the R-curves of wedge-force-loaded double

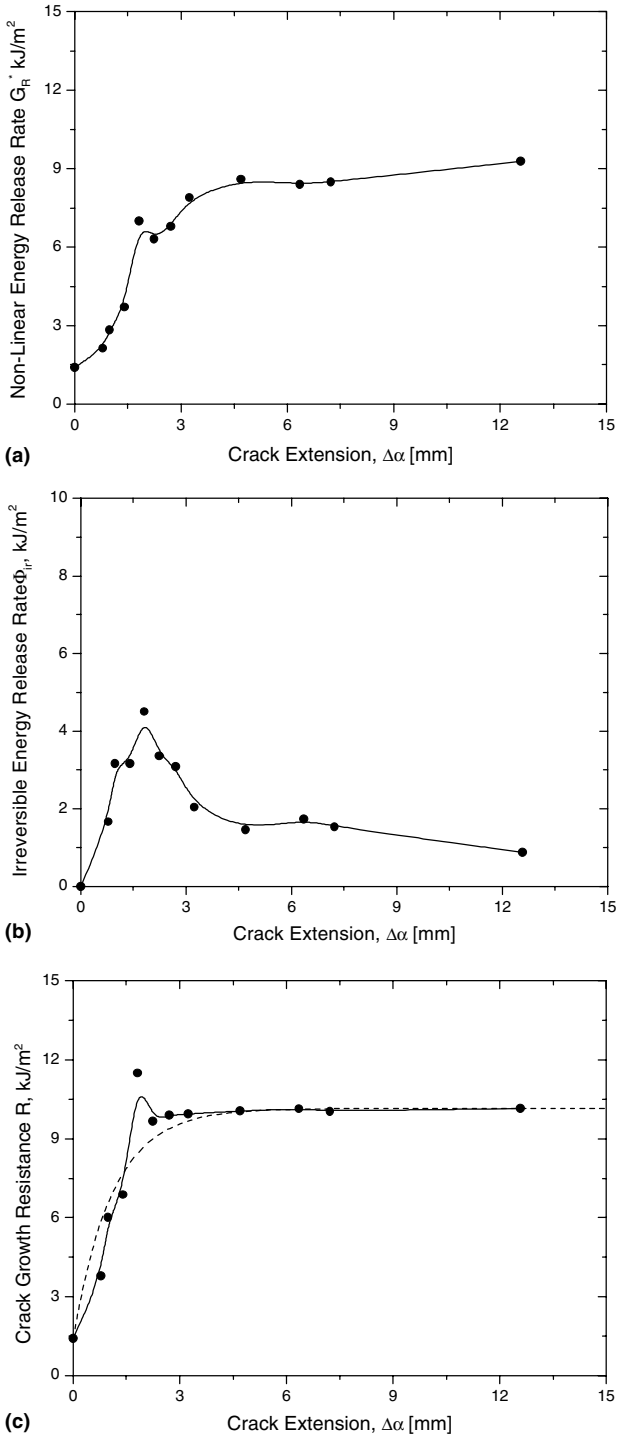

Fig. 11. (a)–(c). C/C CT specimen: G_R^*, Φ_{ir} and the resultant crack growth resistance (R) curve. Symbols represent values obtained from the analysis at each cycle/crack extension, solid lines are spline fits to the data whereas the dashed line represents the idealised R-curve behaviour.

cantilever beam (DCB) specimens [10] and is associated with the angle of rotation of the beam-end. The overshoot region is not related to the development of the bridging zone. The idealised, i.e. without "overshoot", *R*-curve for the CT specimens tested in this study is presented in Fig. 11(c) with a dashed line.

4. CT Specimens: bridging stresses methodology and evaluation

4.1. Bridging stresses evaluation methodology

The bridging law adopted in this study is a power law of the form [13]:

$$\frac{\sigma_b(x)}{\sigma_{max}} = \left[1 - \frac{\delta(x)}{\delta_c}\right]^n \quad \text{with } n \geqslant 0, \tag{16}$$

where x represents the distance from the crack tip, σ_{max} is the value of the bridging stress field at the crack tip (Fig. 12), δ_c is the critical crack opening displacement beyond which bridging fibres fail and n is the toughening exponent, related directly to the bridging mechanism active in the material: a higher n value is associated with a bridging stress profile decreasing with crack extension in a steeper manner. When $n > 1$ the bridging law is concave up whereas when $0 \leqslant n < 1$ the bridging law is concave down. The bridging law is a local law and holds only within the range of the fully developed bridging zone. The parameters $\delta(x)$ and δ_c are represented schematically in Fig. 13.

The values of the local parameters $\delta(x)$ and δ_c can be evaluated by extrapolation of the experimental COD data (measured at the load line, Fig. 13) using the assumption of a linear crack opening versus crack extension profile [12] through the rule of similar triangles (Fig. 13):

$$\delta(x) = \frac{\Delta\alpha}{\alpha}\delta_{exp} \tag{17}$$

which, for the case of the fully developed bridging zone, becomes:

$$\delta_c = \frac{A}{A + \alpha_0}\delta_{exp,c}. \tag{18}$$

In Eq. (18), the value $\delta_{exp,c}$ corresponds to the load-line crack opening displacement when the bridging zone first reaches its saturation value: it can be read off the COD-crack extension curve (Fig. 10(b)) for a crack

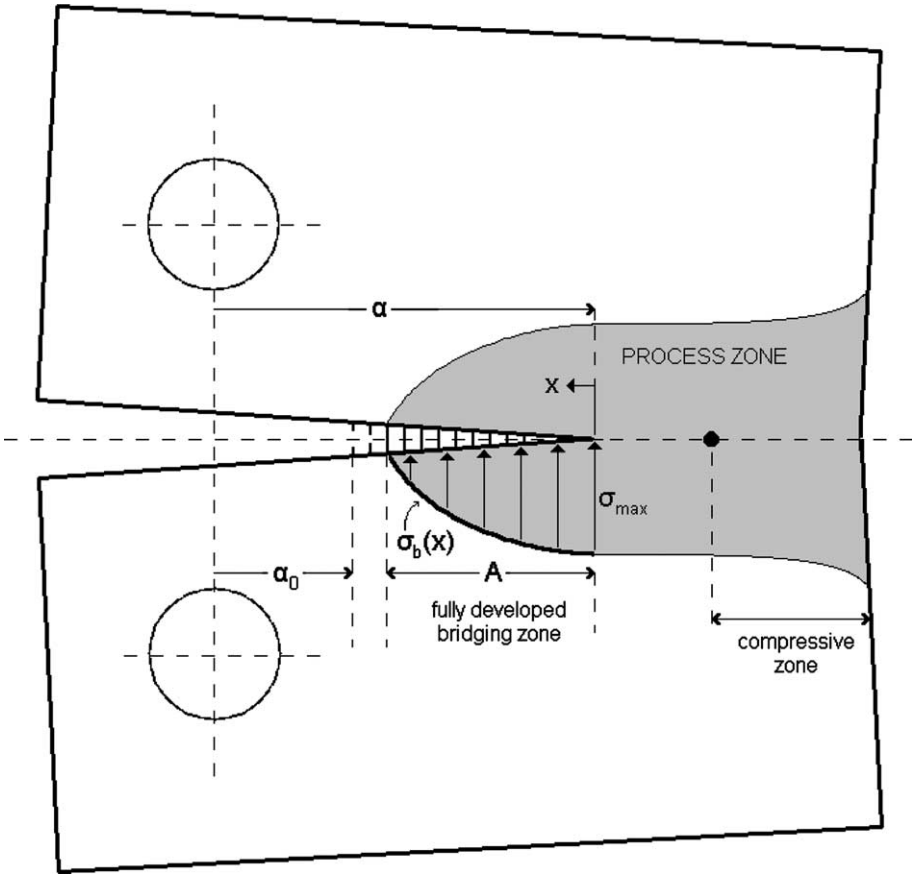

Fig. 12. The bridging zone and law in a CT specimen.

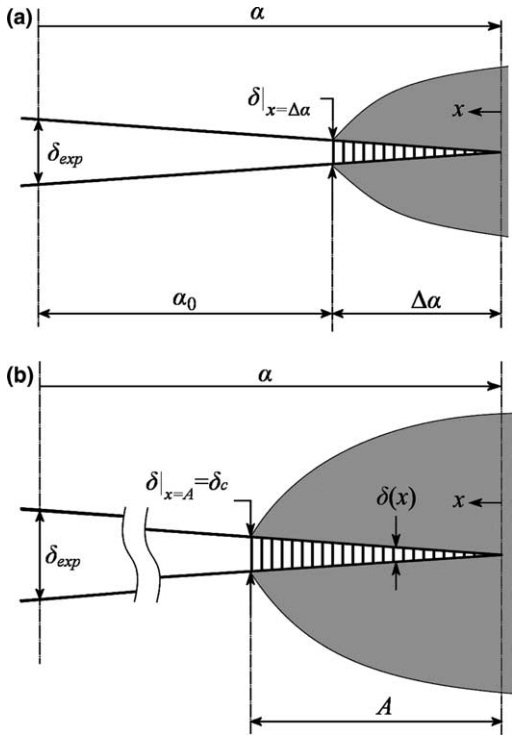

Fig. 13. Schematic representation of the local characteristics of the bridging law (a) during the development of the bridging zone and (b) when the bridging zone has fully developed. δ_{exp} is the experimental crack opening displacement, measured at the load line. The bridging law depicted corresponds to a toughening exponent greater than unity ($n > 1$).

extension equal to the length of the fully developed bridging zone, A.

The calculation of n and σ_{max} uses the same assumption of a linear relation between the crack opening displacement and the crack extension within the fully developed bridging zone:

$$\frac{\Delta\alpha}{A} = \frac{\delta(x)}{\delta_c} \quad \text{for } 0 \leqslant x \leqslant A. \tag{19}$$

Using Eq. (19), Eq. (16) can be re-written as

$$\frac{\sigma_b(x)}{\sigma_{max}} = \left[1 - \frac{\Delta\alpha}{A}\right]^n. \tag{20}$$

The function $\varphi(\Delta\alpha)$ is defined as

$$\varphi(\Delta\alpha) = \int_0^{\Delta\alpha} \frac{\sigma_b(y)}{\sigma_{max}}\, dy. \tag{21}$$

Mai and Hu [12] correlated the difference between $C(\Delta\alpha)$ and $C^*(\Delta\alpha)$ with the bridging stress profile $\sigma_b(x)$ as a function of the distance from the crack tip, x, according to the equation:

$$\frac{\sigma_b(x)}{\sigma_{max}} = -\frac{C^2(\Delta\alpha)}{dC(\Delta\alpha)/d(\Delta\alpha)} \frac{dC^*(x)/dx}{[C^*(x)]^2}. \tag{22}$$

Using Eq. (21) to integrate the right-hand sides of Eqs. (22) and (20) leads to:

$$\varphi(\Delta\alpha) = \frac{C(\Delta\alpha)}{dC/d(\Delta\alpha)}\left[\frac{C(\Delta\alpha)}{C^*(\Delta\alpha)} - 1\right] = \frac{A}{n+1}\left[1 - \left(1 - \frac{\Delta\alpha}{A}\right)^{n+1}\right]. \tag{23}$$

Knowing $C(\Delta\alpha)$ and $C^*(\Delta\alpha)$ one can directly calculate the function $\varphi(\Delta\alpha)$. For $\Delta\alpha = A$, $\varphi(\Delta\alpha)$ reaches its steady-state value φ_∞:

$$\varphi_\infty = \frac{A}{n+1}. \tag{24}$$

Given the length of the fully developed bridging zone, A, from the R-curve, and the value of φ_∞, the toughening exponent n is obtained through Eq. (24).

The parameter σ_{max} can be calculated from the initiation and plateau values of the R-curve, G_{IC} and G_∞, respectively, through the formula:

$$G_\infty - G_{IC} = \int_0^{\delta_c} \sigma_b(\delta)\, d\delta = \frac{\sigma_{max}\delta_c}{n+1}. \tag{25}$$

Finally, the bridging stress profile can be calculated as a functional form of local crack opening displacement, δ, through Eq. (16) or incrementally for each crack extension through Eq. (20) or by differentiating the function $\varphi(\Delta\alpha)$ (Eq. 21):

$$\frac{\sigma_b(x)}{\sigma_{max}} = \frac{d\varphi(\Delta\alpha)}{d(\Delta\alpha)}. \tag{26}$$

Summarising, given the $P(\delta)$, $C(\Delta\alpha)$ and $C^*(\Delta\alpha)$ functions, the bridging stress profile can be calculated following the methodology presented below:

- calculation of the function $\varphi(\alpha)$ using the first side of Eq. (23),
- calculation of the toughening exponent n through Eq. (24) from the plateau value of $\varphi(\Delta\alpha)$, φ_∞ (given the value of A from the R-curve behaviour),
- determination of the critical local crack opening displacement δ_c from the experimental COD-crack extension curve at $\Delta\alpha = A$ using Eq. (18),
- determination of σ_{max} from the R-curve behaviour, the toughening exponent n, the critical local crack opening displacement δ_c and Eq. (25),
- evaluation of the bridging stress field as a function of local crack opening displacement from Eq. (16), or,
- evaluation of the bridging stress field as a function of crack extension from Eq. (20) or Eq. (22).

4.2. Bridging stresses evaluation in CT specimens

The calculated modified compliance for each cycle is plotted together with the compliance calibration curve as a function of crack extension in Fig. 14.

The function $\varphi(\Delta\alpha)$ is calculated by substituting the C and C^* values from Fig. 14 into Eq. (23). The function $\varphi(\Delta\alpha)$ is plotted versus the effective crack extension and the steady-state value of $\varphi_\infty = 3.03$ mm is determined (Fig. 15) by fitting the data with a non-linear regression function of the form $\varphi(\Delta\alpha) = b[c - e^{-d\cdot\Delta\alpha}]$, where b, c and d are constants.

The plateau value, φ_∞, is reached at a crack extension of $\Delta\alpha = A_\varphi = 5.70$ mm, which provides a primary measure of the length of the fully developed bridging zone.

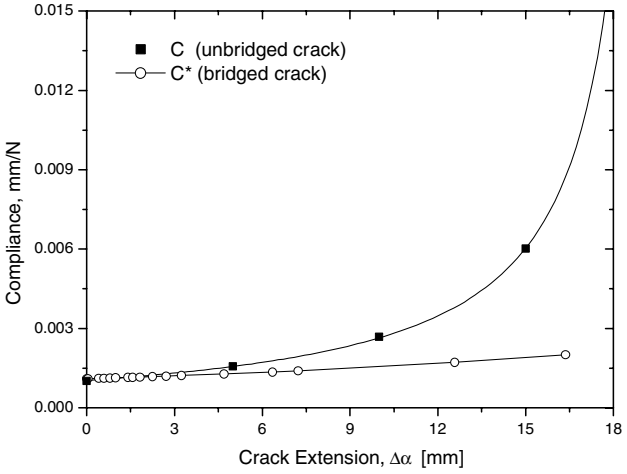

Fig. 14. The compliance as a function of effective crack extension in the presence (C^*) and in the absence of the bridging zone (C). Hollow triangles and circles represent experimental values obtained from the compliance calibration and cyclic loading tests, respectively.

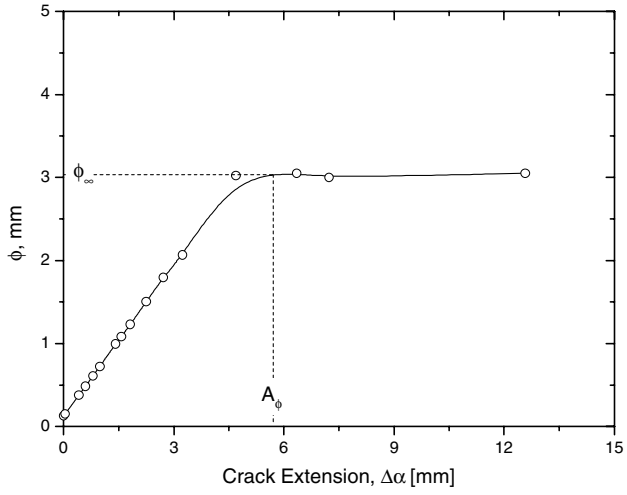

Fig. 15. The function φ as a function of effective crack extension.

Using the R-curve behaviour (Fig. 11(c)) the initiation and plateau values are calculated as: $G_{IC} = 1.40$ kJ/m^2, $G_\infty = 10.1$ kJ/m^2. The length of the fully developed bridging zone, A_R, with respect to the R-curve behaviour, is evaluated by fitting the data of Fig. 11(c) with a non-linear regression function of the form $R(\Delta\alpha) = f[g - e^{-h\cdot\Delta\alpha}]$, where f, g and h are constants. The specific regression does not take into consideration the values of the R-curve within the "overshoot" region, as these values are not associated with the formation of the bridging zone. A value of $A_R = 5.65$ mm is obtained, that agrees well with the value of A_φ. For the purpose of this study, the length of the fully developed bridging zone, A, is assumed equal to the mean value of A_R and A_φ, i.e. $A = 5.675$ mm.

From the steady-state φ_∞ and A values, a toughening exponent value of $n = 0.87$ was obtained through Eq. (24). Using Fig. 10(b) to read a critical load-line-COD value of $\delta_{exp,c} = 1.47$ mm at a crack extension equal to the length of the fully developed bridging zone ($A = 5.675$ mm), the local δ_c was calculated through Eq. (18) to be 0.18 mm. The maximum bridging stress was calculated through Eq. (25) as $\sigma_{max} = 90.3$ MPa. Finally, the bridging stress profile was found by Eq. (20) and plotted as a function of crack extension (Fig. 16) whereas the form of the bridging law was determined through Eq. (16):

$$\sigma_b(x) = 90.3 \cdot \left[1 - \frac{\delta(x)}{0.18}\right]^{0.87}. \tag{27}$$

The bridging law is represented schematically in Fig. 16.

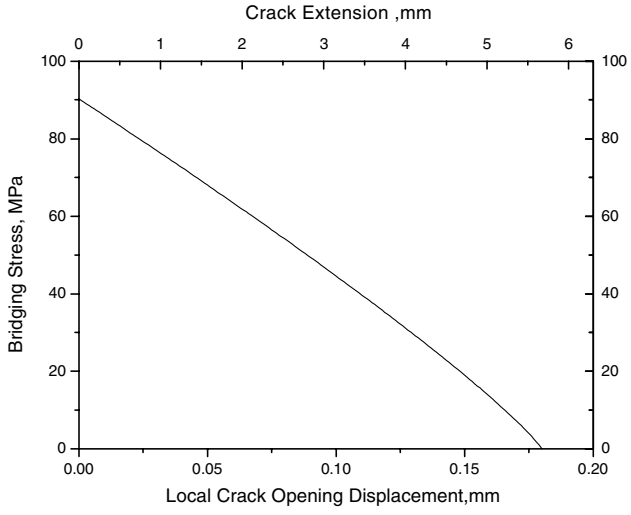

Fig. 16. CT specimen: the crack-face bridging stress as a function of crack extension and local crack opening displacement (local bridging law).

5. Den specimens: *R*-curve and bridging stresses

5.1. Calculation of the effective crack opening

In DEN tests, the characteristic parameter that quantifies the irreversible damage caused to the material by the total energy input is the crack opening, i.e. the separation of the two crack faces, rather than crack extension, which is the preferred parameter in the fracture of CT specimens. Crack opening is defined as the non-elastic displacement of the system and is directly associated, similarly to CT specimens, with the existence of a bridging zone. Hence, the load carried by the composite when a crack covers the total width between the notches is the bridging load, F_{br}. The total crack opening can be calculated by subtracting the elastic displacement from the total recorded displacement. If D_0 is the initial slope of the measured load–displacement curve, the total crack opening, e, is obtained from the instantaneous load–displacement pairs (F,d) through:

$$e(d) = d - \frac{F(d)}{D_0}. \tag{28}$$

Fig. 17 is a graphical illustration of the elastic displacement correction of Eq. (28). Since displacement, d, is measured directly over the crack faces of the DEN specimen, the crack opening calculated through Eq. (28) has a local character and will be refer to, hereon, as "local crack opening displacement".

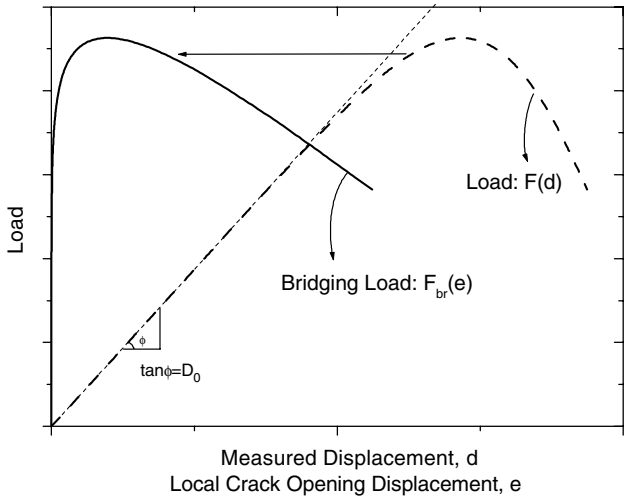

Fig. 17. Conversion of the measured load–displacement curve to a bridging load–local COD curve using elastic displacement correction.

5.2. Crack growth resistance curve and bridging stresses

Under the assumption that non-elastic contributions to the measured displacement directly stem from the presence of the bridging zone, the bridging work that contributes to the increase of crack opening resistance can be calculated as the area under the bridging load versus crack opening curve (Fig. 18):

$$R = \Delta G = \int_0^e \frac{F_{\mathrm{br}}(e)}{t \cdot (w - 2\alpha_0)}\, \mathrm{d}e. \tag{29}$$

In Eq. (29), t is the specimen thickness and $t \cdot (w - 2\alpha_0)$ represents the area of the bridging zone, i.e. the cross-section of the bridged ligament of the specimen. Accordingly, the integrand in Eq. (29) represents the nominal bridging stress, $\sigma_{\mathrm{br}}(e)$,

$$\sigma_{\mathrm{br}}(e) = \frac{F_{\mathrm{br}}(e)}{t \cdot (w - 2\alpha_0)}. \tag{30}$$

Eq. (30) is the directly measured (real) bridging law for DEN specimens. The directly measured bridging laws and the corresponding *R*-curves for the DEN specimens are presented in the following section.

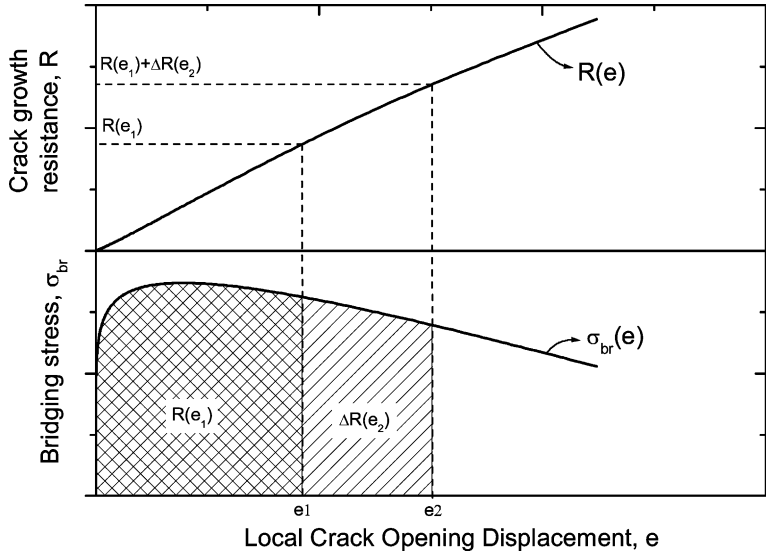

Fig. 18. DEN specimens: evaluation of the *R*-curve from the bridging load-crack opening curve.

6. Discussion

In search for material intrinsic parameters that characterise the fracture behaviour of the C/C composite, the attention is focused to the two primary candidates: the *R*-curve and the bridging law. Crack growth in CT and DEN specimens refers to different physical phenomena, namely *crack propagation parallel* to the direction of the characteristic specimen dimension, W, in CT specimens, and *crack-face opening normal* to the direction of W in DEN specimens. Moreover, in contrast to the CT configuration where damage is dominated by the formation, development and self-similar translation of the bridging zone, in a DEN test matrix cracking between the notches develops rapidly and damage is dominated by incremental fibre failure within the bridging zone which remains geometrically fixed throughout the test.

The authors believe that it is possible to compare the two configurations by identifying common parameter(s) that quantify the damage mechanisms active in the two configurations. Such a parameter is the local crack opening displacement, which, in a DEN test, is calculated through the elastic correction of the measured displacement (Eq. (28)) and, in a CT test, is calculated from the experimental load-line COD measurements through Eq. (17).

6.1. Comparison of bridging laws

The bridging law calculated for the CT specimens through the compliance approach is plotted as a function of local crack opening displacement along with the directly measured bridging laws for DEN specimens with different notch-to-width ratios in Fig. 19.

By examination of Fig. 19 it is obvious that the bridging law for the CT specimens is different from that of the DEN specimens, implying that the distribution of bridging stresses in the bridging zone during damage evolution depends on specimen geometry. Moreover, by examination of the bridging laws for the DEN specimens in Fig. 19 it is observed that specimens with higher initial notch-to-width ratios are associated with higher values of bridging stresses. Hence, not only is the bridging law affected by the geometry of the material, but also by its dimensional characteristics. A dimensional- and configurational-dependent property, the bridging law cannot serve as an intrinsic parameter for the characterisation of the fracture behaviour of this type of composite.

6.2. Comparison of R curves

The crack growth resistances of CT and of DEN specimens with different initial notch-to-width ratios are plotted as a function of local COD for both configurations in Fig. 20 which represents, essentially, a comparison of the capacities of the two bridging zones (CT and DEN) to provide resistance to further crack opening (and hence also crack growth) within a loaded specimen.

By examination of Figs. 19 and 20, it is observed that the R_0 and R_∞ values for the DEN specimen with an initial notch-to-width ratio of 0.5 are slightly higher than the corresponding values for specimens with 0.4 and 0.6 ratios. However, given the very small difference between the data of the individual values, mean values of R_0 and R_∞, representative of all three notch-to-width ratios, were calculated as: $R_0 = 1.24\ \mathrm{kJ/m^2}$ and $R_\infty = 9.10\ \mathrm{kJ/m^2}$.

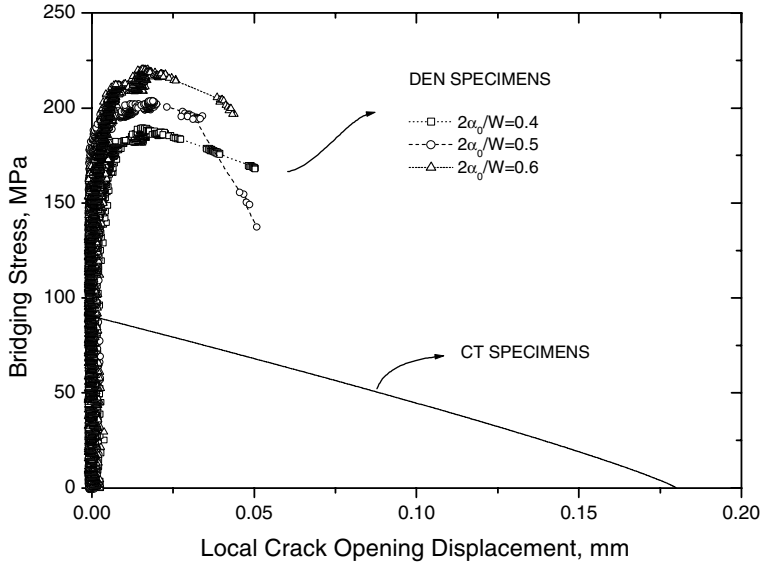

Fig. 19. C/C DEN specimens: the directly measured bridging laws. Calculated and real bridging laws for the CT and DEN configurations, respectively.

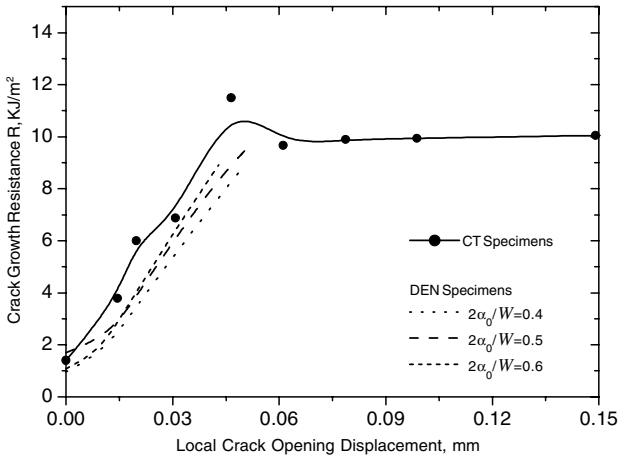

Fig. 20. C/C DEN specimens: crack growth resistance as a function of crack opening. *R*-curves of CT and DEN specimens as a function of local crack opening displacement. Solid cycles represent experimental data from cyclic loading of CT specimens. The span of the *x*-axis is equal to the local δ_c value of the CT specimen corresponding to the length of the fully developed bridging zone.

From Fig. 20 it is observed that the *R*-curves of CT and DEN specimens compare favourably within the bridging zone development regime (rising part of the *R* curve) so that the two configurations have similar capacities with respect to crack growth resistance over the same range of local crack opening displacements. Of course, it is the absence of a self-similar crack propagation feature in the DEN configuration that restricts *R* curve comparison to only within this first regime. Inasmuch as it is a fracture parameter with configuration-independent (and thus also dimension-independent) values, the *R*-curve appears to act as a material-intrinsic property.

6.3. Remarks

It can be shown that a toughening exponent value of $n = 0$ signifies a linearly rising *R*-curve behaviour whereas, for $n > 0$, the *R*-curve is concave-down, with a profile increasing monotonically in a more steeper manner with increasing toughening exponent. As far the bridging law is concerned, the value of the toughening exponent $n = 0.87$ calculated for the CT specimens implies that the bridging stresses are an almost linear function of crack opening displacement (Fig. 19) and crack extension (Fig. 16). This is also observed in the directly measured bridging law for the DEN specimens (Fig. 19) and is also consistent with an almost-linear shape of the *R*-curves (Fig. 20) through Eqs. (25) and (29) for the CT and DEN configuration, respectively. A discussion on the effect of the toughening exponent value on the bridging law is offered in [13].

The finding that the *R*-curve, rather than the bridging law, is a material-intrinsic fracture parameter leads to the question of the applicability of LSB conditions in the investigated C/C composite. In fact, by examination of Fig. 19 it is evident that the local crack opening is only a very small fraction of the characteristic specimen dimension, *W*, for both configurations (0.5% and 0.4% for the DEN and CT specimens, respectively), suggesting that SSB conditions apply rather than LSB. Another observation that supports the validity of this remark is the fact that crack extension in the CT specimens is not considerable – for example the length of the fully developed bridging zone is ca. 9% of the width of the CT specimen. The C/C composite family has been characterised in the literature as a Class-III family [3], i.e. one whose fracture exhibits multiple shear matrix cracking and not distinct crack advance and bridging. The toughening mechanisms in such systems are neither crack bridging nor *R*-curve effects. However, the I–III classification of composites' fracture is too general to characterise the whole of large composite families as the C/C family. For example, distinct crack advance and bridging may coexist with shear matrix cracking in an otherwise Class III composite. This has been proven in the work of Goto et al. [9] who directly identified crack extension in a C/C composite using a travelling microscope and of Pappas and Kostopoulos [14] who ultrasonically and optically confirmed the presence of crack growth and bridging in the same 2D C/C woven composite as the one used in this study. At the same time it should not be overlooked that the crack extension calculated for the CT specimens in this study is based on the notion of an "effective crack length" where the total damage forming and evolving in the material during testing is assumed to be equivalent to a distinct crack propagating through the matrix.

It is hence concluded that the investigated C/C woven composite does exhibit crack propagation and bridging however not of large scale and that the *R*-curve of the material can be used to characterise its fracture behaviour independently of specimen configuration or dimension.

7. Conclusions

CT and DEN specimens of a woven C/C composite were tested under cyclic and monotonic tensile loading conditions and the crack growth resistance curves for each configuration were obtained using a compliance approach (CT specimens) and a direct elastic displacement correction approach (DEN specimens). Although the plateau value of the *R*-curve for the CT specimens spanned a larger range of crack opening compared to the DEN case as a direct result of the self-similar propagation of the bridging due to interaction with the compressive zone, the *R*-curves evaluated for the two different configurations/methodologies were similar

within the bridging zone development regime. The initiation and plateau values of ca. $R_0 \sim 1.3$ kJ/m^2 and $R_\infty \sim 9.5$ kJ/m^2, respectively, as well as the shape of the R-curves within that regime were similar for both CT and DEN specimens. In contrary, the evaluated bridging laws differed in shape between the two configurations. These observations lead to the conclusion that the composite used in this study exhibits SSB and, as such, its fracture behaviour is characterised by the R-curve which is an intrinsic property of the material.

References

[1] Lamic P, Boury D. Ceramic matrix composites parts design. AGARD-R-795 1993, Introduction of ceramics into aerospace structural composites.

[2] Kostopoulos V, Pappas YZ. Toughening mechanisms in long fibre ceramic matrix composites. In: Kelly A, Zweben C, editors. Comprehensive composite materials, vol. 1. Amsterdam: Elsevier; 2000. p. 95–114.

[3] Evans AG, Zok FW. Review: the physics and mechanics of fibre-reinforced brittle matrix composites. J Mater Sci 1994; 29:3857.

[4] Kostopoulos V, Markopoulos YP. On the fracture toughness of ceramic matrix composites. Mater Sci Eng A 1998;250(2):303–12.

[5] Cox BN. Extrinsic factors in the mechanics of bridged cracks. Acta Metall Mater 1991;39:1189–201.

[6] Suo Z, Bao G, Fan B. Delamination R-curve phenomena due to damage. J Mech Phys Solids 1992;40:1–16.

[7] Brenet P, Conchin F, Fantozzi G, Reynaud P, Rouby D, Tallaron C. Direct measurements of crack-face bridging tractions: a new approach to the fracture behaviour of ceramic/ceramic composites. Compos Sci Technol 1996;84(6):817–23.

[8] Sorensen BF, Jacobsen TK. Large-scale bridging in composites: R-curves and bridging laws. Composites A 1998;29: 1443–1451.

[9] Goto K, Hatta H, Takahashi H, Kawada H. Effect of shear damage on the fracture behavior of carbon–carbon composites. J Am Ceram Soc 2001;84(6):1327–33.

[10] Jacobsen TK, Sorensen BF. Mode-I intra- laminar crack growth in composites – modelling of R-curves from measured bridging laws. Composites A 2001;32:1–11.

[11] Rausch G, Kuntz M, Gratwohl G. Determination of the in situ fiber strength in ceramic-matrix composites from crack-resistance evaluation using single-edge notched-beam tests. J Am Ceram Soc 2000;84(6):2762–8.

[12] Hu XZ, Mai YW. General Method for determination of crack-interface bridging stresses. J Mater Sci 1992;27: 3502–10.

[13] Foote RML, Mai YW, Cotterell B. Crack growth resistance curves in strain-softening materials. J Mech Phys Solids 1986;34(6):593–607.

[14] Pappas YZ, Kostopoulos V. Toughness characterization and acoustic emission monitoring of a 2-D carbon/carbon composite. Eng Fract Mech 2001;68:1557–73.